

Article

Mass Transfer Behaviors and Battery Performance of a Ferrocyanide-Based Organic Redox Flow Battery with Different Electrode Shapes

Pengfei Zhang, Xi Liu, Junjie Fu and Fengming Chu * 

College of Mechanical and Electrical Engineering, Beijing University of Chemical Technology, Beijing 100029, China

* Correspondence: cfm@mail.buct.edu.cn

Abstract: The ferrocyanide-based organic redox flow battery (ferrocyanide-based ORFB), based on electrochemistry, has become a potential energy storage technology due to its low price, eco-friendliness, safety, and convenience. However, its low efficiency and poor mass transfer performance hinder the application of the ORFB. The influence of the electrode shape (trapezoid, sector, and rectangle) on the mass transfer and battery performance are studied based on a numerical model, which is verified by the experiments. The results show that battery performance of the trapezoid electrode is better than that of the sector and rectangle electrode. The discharge voltage of the rectangle battery is the lowest, and the discharge voltage of the trapezoid battery is the highest. The discharge voltage of the rectangle battery is 4.47% lower than that of the trapezoid battery. The uniformity factor value of the trapezoid battery is 26.9% higher than that of the rectangle battery. The trapezoid shape is the best design for the electrode, contributing to the application of the ferrocyanide-based ORFBs.

Keywords: energy storage; numerical model; discharge voltage; electrode shape; mass transfer



Citation: Zhang, P.; Liu, X.; Fu, J.; Chu, F. Mass Transfer Behaviors and Battery Performance of a Ferrocyanide-Based Organic Redox Flow Battery with Different Electrode Shapes. *Energies* **2023**, *16*, 2846. <https://doi.org/10.3390/en16062846>

Academic Editor: Carlos Miguel Costa

Received: 25 January 2023

Revised: 26 February 2023

Accepted: 9 March 2023

Published: 19 March 2023



Copyright: © 2023 by the authors. Licensee MDPI, Basel, Switzerland. This article is an open access article distributed under the terms and conditions of the Creative Commons Attribution (CC BY) license (<https://creativecommons.org/licenses/by/4.0/>).

1. Introduction

As the climate change has become increasingly serious over past decades, wind energy and solar energy have received greater attention. The disadvantages of intermittent discontinuity and instability hinders their large-scale application. Energy storage technology, based on the electrochemistry, is regarded as one of the best methods to solve this problem [1–3]. With its safety, high efficiency, and scalability, the redox flow battery stands out among many large-scale energy storage technologies [4]. The ferrocyanide-based ORFB offers the advantages of lower cost and improved environmental protection [5,6], making it increasingly popular [7–9]. However, the low solubility of the organics leads to poor mass transfer behaviors in the porous electrodes, which results in the low battery performance of the ferrocyanide-based ORFB. It is significant to investigate the mass transfer performance in the porous electrodes for the commercial application of this technology.

It is well known that the transport and distribution of the reactants are influenced by the flow fields of the electrodes [10]. In the past few decades, researchers have conducted numerous investigations on electrodes with different flow fields. Xu et al. [11] studied the battery without a flow field and with a serpentine flow field, discovering that the energy efficiency of the battery with the serpentine flow field was 5% higher than that of the battery without a flow field. Macdonald et al. [12] investigated the battery performance of a interdigital flow field and a serpentine flow field using a two-dimensional model based on Darcy's law and reported that the pressure drop of the interdigital flow field was lower than that of the serpentine flow field. Luo et al. [13] combined the serpentine flow field with the interdigital flow field to obtain a new flow field, determining that the system energy efficiency of the new flow field is 2%–20% higher than that of the interdigital or serpentine flow field. Ali et al. [14] investigated the influence of the number of serpentine

flow field channels on the all-vanadium flow battery performance and pointed out that the quadruple serpentine design resulted in the highest power-based efficiency. Lu et al. [15] studied a blocked serpentine flow field and reported that 1.4 mm was the most appropriate block height for all vanadium flow batteries. Lee et al. [16] researched the effects of the serpentine channel size on the all-vanadium flow battery performance and reported that a smaller channel size could lead to a high power-based efficiency. Lee et al. [16] also pointed out that the higher electrolyte flow rate could result in better battery performance.

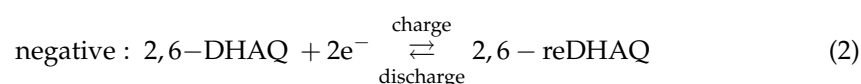
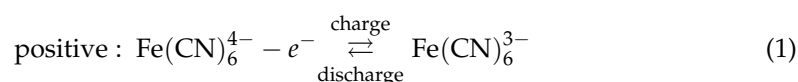
Besides the researches on the flow fields, the influence of the electrode structure on the battery performance is another research hotspot. Chu et al. [17] studied the effect of electrode shape (trapezoid, sector, rectangle) on battery performance, discovering that the battery and mass transfer performance of the sector-shaped electrode were the best. However, the flow fields were not investigated in the study of Chu et al. [17]. Yin et al. [18] designed a 'leaf' shaped electrode and compared it with the bipolar plate interdigital flow field and no flow field. The result showed that the pressure drop of the 'leaf' shaped electrode was lower than that of either the interdigital flow field or no flow field. Gurieff et al. [19] investigated the performance of the battery with three different electrode structures (trapezoid, sector, and rectangle) and concluded that the different electrode structures could lead to different battery performance and mass transfer behavior. Ali et al. [20] studied the effect of electrode thickness on the battery performance, and the results showed that when the electrode thickness was 1 mm, the maximum efficiency of the battery was 96.8%. Lu et al. [21] designed a battery with an asymmetric electrode structure. Their research found that this electrode can reduce the capacity reduction of the vanadium ions, increasing the overall energy efficiency from 83% to 87.7%.

In reference [14], the influence of electrode shape on the ferrocyanide-based ORFB battery performance and mass transfer process were studied. However, the electrodes in reference [14] are without flow fields. The flow fields play important roles in the mass transfer process. Therefore, it is important to investigate the influence of the electrode shape, with flow fields, on the mass transfer behaviors in the ferrocyanide-based ORFB. In the previous research, most studies concentrated on the flow fields. Few investigations were conducted on the influence of the electrode shape with flow fields. In this paper, the influence of the electrode shape (trapezoid, sector, and rectangle), with the electrode equipped with flow fields, on the mass transfer and battery performance is investigated. The charge-discharge voltage, over voltage, polarization curve, uniformity factor, average concentration, power, and efficiency of the three kinds of batteries are presented.

2. Model

The conventional ferrocyanide-based ORFB, consisting of an ion exchange membrane, a positive electrode, negative electrodes, two collectors, two pumps for circulating electrolyte liquid, and two electrolyte flow tanks, is shown in Figure 1. The type of ion exchange membrane in this work is a Nafion[®]212 membrane, and the supporting electrolyte is the KOH. The electrolyte was transferred to the porous electrode by the pumps, and the porous electrode can provide more reaction areas for the electrolyte charging and discharging of the electrode. Then, the electrolyte is pumped from the electrode to the tank. Figure 1 shows the three electrode shapes (trapezoid, sector, and rectangle).

The electrolytes used in this organic redox flow battery are presented as follows. The negative electrolyte is 2,6-DHAQ/2,6-reDHAQ, and the positive electrolyte is $\text{Fe}(\text{CN})_6^{4-}/\text{Fe}(\text{CN})_6^{3-}$. The electrochemistry reactions occurring in the charging and discharging process are presented as follows:



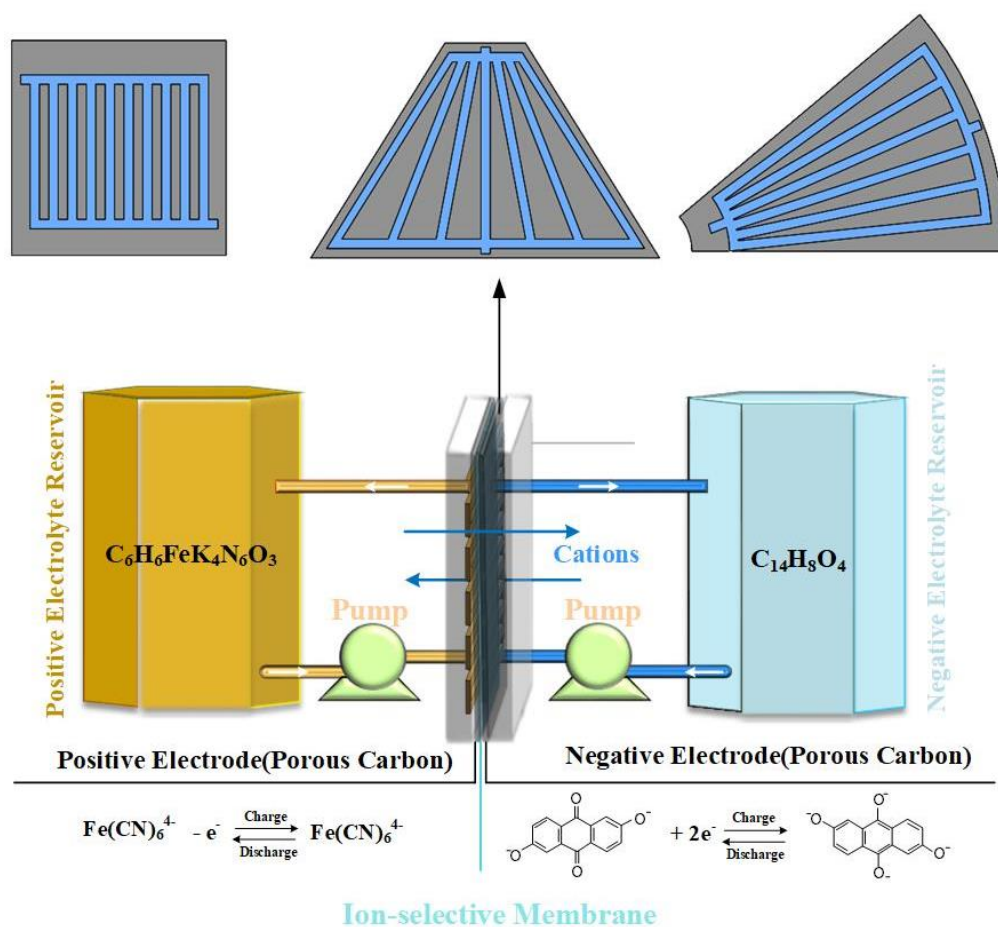


Figure 1. Schematic diagram of the organic flow battery and a three-dimensional sketch of the ferrocyanide-based ORFBs.

In this paper, a three-dimensional steady-state model of the organic redox flow battery is built, and the influences of the different electrode shapes (trapezoid, sector, rectangle) on the battery performance and mass transfer behaviors are investigated. However, the mass transfer process and the coupling of hydrodynamics are very complex. To make the model simple and accurate, the following reasonable assumptions are made:

- (1) It is assumed that only K^+ can pass through the ion exchange membrane.
- (2) It is assumed that the temperature of all regions of the ferrocyanide-based ORFBs is equal and distributed uniformly along all directions of the electrode and the film.
- (3) Side effects are ignored.
- (4) It is assumed that the electrolyte in the water tank is completely mixed.
- (5) The electrolytes are incompressible fluids and diluted solutions.

2.1. Transportation in the Electrode

During battery charging and discharging, the ions present on the positive side electrode are $Fe(CN)_6^{4-}/Fe(CN)_6^{3-}$ and K^+/OH^- ions. The ions in the negative electrode side electrode are 2,6-DHAQ/2,6-reDHAQ and K^+/OH^- ions. Each species i in the positive and negative electrode follows the following formula:

$$\nabla \cdot \vec{N}_i = -S_i \quad (3)$$

where S_i is the source term of specie i , which can be seen in Table 1. The molar flux N_i of each species i can be obtained by the Nernst–Planck equation:

$$\vec{N}_i = -D_i^{\text{eff}} \nabla c_i - z_i w_i c_i F \nabla \phi_1 + \vec{u} c_i \tag{4}$$

Table 1. Kinetic and electrochemistry parameters used in the simulation.

| Parameter | Symbol | Value | Source |
|--|-----------------------------------|------------------------|-----------|
| Specific surface area (m^{-1}) | a | 2.5×10^5 | measured |
| Diffusion coefficient of 2,6-reDHAQ (m^2/s) | $D_{2,6\text{-reDHAQ}}$ | 4.8×10^{-10} | Ref. [13] |
| Diffusion coefficient of 2,6-DHAQ (m^2/s) | $D_{2,6\text{-DHAQ}}$ | 4.8×10^{-10} | Ref. [13] |
| Diffusion coefficient of $\text{Fe}(\text{CN})_6^{4-}$ (m^2/s) | $D_{\text{Fe}(\text{CN})_6^{4-}}$ | 6.89×10^{-10} | Ref. [22] |
| Diffusion coefficient of $\text{Fe}(\text{CN})_6^{3-}$ (m^2/s) | $D_{\text{Fe}(\text{CN})_6^{3-}}$ | 7.20×10^{-10} | Ref. [22] |
| Diffusion coefficient of K^+ (m^2/s) | D_{K^+} | 1.96×10^{-9} | Ref. [13] |
| Diffusion coefficient of OH^- (m^2/s) | D_{OH^-} | 5.27×10^{-9} | Ref. [13] |
| Operating temperature (K) | T | 297.3 | - |
| Electrode conductivity (S/m) | σ_s | 1000 | Ref. [23] |
| Membrane conductivity (S/m) | σ_m | 10 | Ref. [23] |
| Anodic transfer coefficients | α^+ | 0.5 | Ref. [24] |
| Cathodic transfer coefficient | α^- | 0.5 | Ref. [24] |
| Rate constant, negative reaction (m/s) | k_{neg} | 7×10^{-6} | Ref. [24] |
| Rate constant, positive reaction (m/s) | k_{pos} | 6×10^{-5} | Ref. [24] |
| Standard potential of negative reaction (V) | $E_{0,\text{neg}}$ | -0.71 | Ref. [24] |
| Standard potential of positive reaction (V) | $E_{0,\text{pos}}$ | 0.33 | Ref. [13] |
| Density of active species of the negative electrode | ρ_{neg} | 1080 | measured |
| Density of active species of the positive electrode | ρ_{pos} | 1200 | measured |
| Dynamic viscosity of the negative electrode (Pa·s) | μ_{neg} | 1.17×10^{-3} | Ref. [23] |
| Dynamic viscosity of the positive electrode (Pa·s) | μ_{pos} | 1.09×10^{-3} | Ref. [23] |
| Pump efficiency | φ | 0.9 | Ref. [23] |
| Outlet pressure (kPa) | p_{out} | 101.3 | - |

D_i^{eff} is the effective diffusion coefficient of specie i , c_i is the concentration of specie i , and z_i is the valence of specie i . The w_i represents the ion mobility. F is a constant of the Faraday exponent, and ϕ_1 is the potential of the electrolyte, respectively. The effective diffusion coefficient of specie i can be obtained by the Bruggeman equation.

$$D_i^{\text{eff}} = \varepsilon^{3/2} D_i \tag{5}$$

where ε is the porosity of the porous electrode, and D_i is the diffusion coefficient of species i in electrode. K is the permeability of the electrode, given by Kozeny–Carman equation:

$$K = \frac{d_f^2 \varepsilon^3}{K_f (1 - \varepsilon)^2} \tag{6}$$

where d_f is the pore diameter of the carbon fiber. K_f is the Kozeny–Carman constant, which was set to 4.89.

The formula of the ionic current density in the porous electrode caused by the movement of the point ions in the electrolyte solution is as follows:

$$\vec{I}_1 = F \sum_i z_i \vec{N}_i \tag{7}$$

2.2. Transport in the Membrane

The type of ion exchange membrane was a Nafion[®] 212 membrane, and the supporting electrolyte was the KOH. Only K^+ ion was allowed to pass through the ion exchange membrane, and the other ions are ignored. Thus, the molar flux of K^+ can be obtained by the following formula:

$$\vec{N}_{\text{K}^+} = -\frac{\sigma_m}{F} \nabla \phi_m \tag{8}$$

where σ_m and ϕ_m are the conductivity and potential of the film.

2.3. Electrochemical Kinetics

The overvoltage generated by the electrochemical reaction inside the positive electrode and the negative electrode is expressed by η_n and η_p and can be obtained by the following formula:

$$\eta_n = \phi_{s,n} - \phi_{l,n} - E_{eq,n} \quad (9)$$

$$\eta_p = \phi_{s,p} - \phi_{l,p} - E_{eq,p} \quad (10)$$

$E_{eq,p}$ and $E_{eq,n}$ in the formula represent the open-circuit voltage of positive and negative reactions. $E_{eq,n}$ and $E_{eq,p}$ can be solved by the Nernst equation.

$$E_{eq,n} = E_{0,n} + \frac{RT}{nF} \ln\left(\frac{C_{2,6-DHAQ}}{C_{2,6-reDHAQ}}\right) \quad (11)$$

$$E_{eq,p} = E_{0,p} + \frac{RT}{nF} \ln\left(\frac{C_{Fe(CN)_6^{3-}}}{C_{Fe(CN)_6^{4-}}}\right) \quad (12)$$

where $E_{0,p}$ and $E_{0,n}$ are the typical equilibrium potentials of positive and negative electrochemical reactions.

2.4. Boundary Conditions

The flow rate of electrolyte at the inlet of the positive electrode and negative electrodes is set to \vec{u} , and the outlet pressure is specified as standard atmospheric pressure. The outlet pressure is set to $p = p_{out}$. The Neumann condition is set on all the boundary pressures, except for at the inlet and outlet.

$$p \cdot \vec{n} = 0 \quad (13)$$

On the negative side of the electrode, the potential value at the connection between the electrode and the current collector is set to zero.

At the inlet of the flow field, the initial concentration of each species condition is set as follows:

$$c_i = c_{i,0} \quad (14)$$

2.5. Battery Performance Parameters

The overall electrolyte concentration on the negative side of the battery is set to c_0 , and the electrolyte concentration on the positive side is set to c_1 . In order to observe the electrolyte concentration in the battery, during charging and discharging, the parameter SOC is defined as follows:

$$C_{2,6-reDHAQ} = c_0 \text{SOC} \quad (15)$$

$$C_{DHAQ} = c_0 \cdot (1 - \text{SOC}) \quad (16)$$

$$C_{Fe(CN)_6^{4-}} = c_1 \cdot (1 - \text{SOC}) \quad (17)$$

$$C_{Fe(CN)_6^{3-}} = c_1 \text{SOC} \quad (18)$$

In order to study the performance of three kinds of batteries with different shapes, the charging and discharging voltage of the battery is solved by the following formula:

$$E_{ch} = (E_{eq,pos} - E_{eq,neg}) + (|\eta_{pos}| + |\eta_{neg}|) + I_{avg} AR_{ba} \quad (19)$$

$$E_{dis} = (E_{eq,pos} - E_{eq,neg}) - (|\eta_{pos}| + |\eta_{neg}|) - I_{avg} AR_{ba} \quad (20)$$

In this paper, the method of quantitative analysis is adopted to calculate the uniformity of the electrolyte concentration distribution in the electrode. The uniformity coefficient of distribution of each species i is set as follows:

$$U = 1 - \frac{1}{c_{i,ave}} \sqrt{\frac{1}{V} \iiint (c_i - c_{i,ave})^2 dV} \quad (21)$$

where $c_{i,ave}$ is the average concentration of active materials in the solid electrode, and V is the volume of the solid electrode. Owing to the irreversible nature of the electrode reaction, there is a transfer limitation of the active species in the electrode and a loss of battery power caused by the resistance in the battery, namely P_{loss} , which can be found in our previous work [17].

2.6. Digital Details

In this paper, the secondary current distribution, the transfer of diluted species, and the physical field of the Brinkman equation equipped with steady-state numerical solution are set in COMSOL 5.5. The positive field, negative field, and membrane domain are defined with corresponding variables in the COMSOL Multiphysics 5.5 software. The relative tolerance is specified as 1.5×10^{-6} , and the maximum number of iterations is 150, using the PARDISO solver.

2.7. Model Validation

The experiments are conducted to verify the reliability of the numerical model. In the experiment, the flow field of the ferrocyanide-based ORFB is serpentine shaped, and the geometric size of the experimental electrode is 20 mm \times 20 mm \times 4 mm. The material used for the experimental electrode is graphite felt. The current density is 100 mA/cm². The inlet flow of the electrolyte is set at 60 mL/min. The active ion concentration of the catholyte is set at 100 mol/m³, and the active ion concentration of the anolyte is set at 200 mol/m³. Other detailed experimental parameters can be seen in Tables 1 and 2. The comparison between the numerical results and experimental data is shown in the Figure 2. Figure 2 shows that the simulated and experimental charge-discharge voltage matches the entire charge-state cycle (SOC from 0.1 to 0.9), with a maximum error of 3.9%, which occurs during the discharge process, and the overall average error is less than 2%, indicating that the three-dimensional numerical model established in this paper is accurate and reliable.

Table 2. Geometric and operation parameters used in the experiments.

| Parameter | Symbol | Value |
|--|------------------|-------|
| Length of the electrode (mm) | L_e | 20 |
| Width of the electrode (mm) | W_e | 20 |
| Height of the electrode (mm) | H_e | 4 |
| Length of the membrane (mm) | L_m | 20 |
| Width of the membrane (mm) | W_m | 20 |
| Height of the membrane (mm) | H_m | 0.05 |
| Width of the flow field (mm) | W_c | 0.8 |
| Height of the flow field (mm) | H_c | 0.8 |
| Initial concentration of 2,6-reDHAQ (mol/m ³) | $c_{2,6-reDHAQ}$ | 10 |
| Initial concentration of 2,6-DHAQ (mol/m ³) | $c_{2,6-DHAQ}$ | 90 |
| Initial concentration of $Fe(CN)_6^{4-}$ (mol/m ³) | $c_{Fe(CN)64^-}$ | 20 |
| Initial concentration of $Fe(CN)_6^{3-}$ (mol/m ³) | $c_{Fe(CN)63^-}$ | 180 |
| K^+ concentration in half-cell (mol/m ³) | c_{K^+} | 1000 |
| OH^- concentration in half-cell (mol/m ³) | c_{OH^-} | 1000 |
| Porosity of the electrode | ε | 0.9 |
| Applied current density (mA/cm ²) | I | 100 |
| Inlet electrolyte flow rate (mL/min) | Q_0 | 60 |

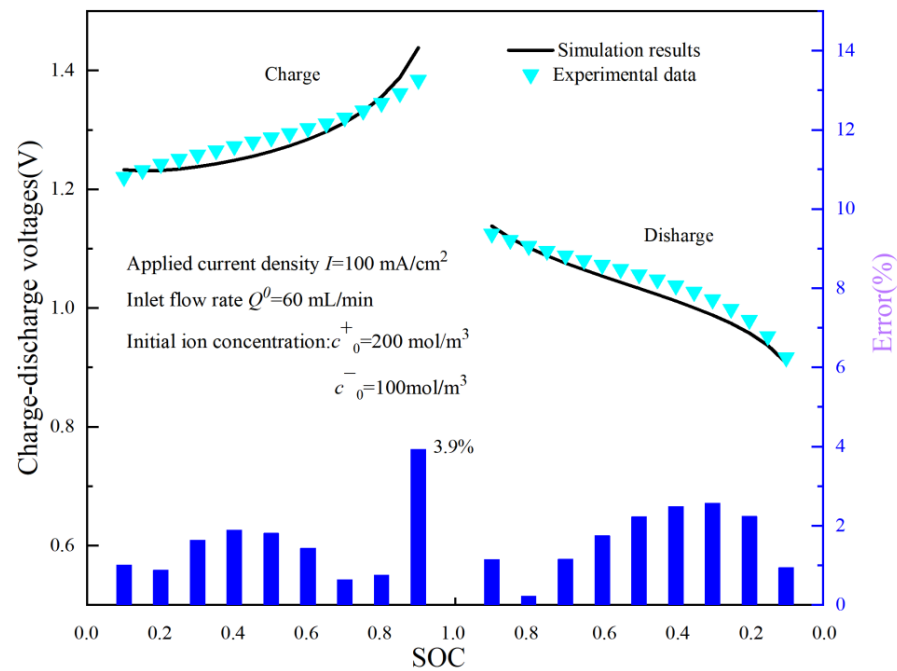


Figure 2. Comparisons between numerical and experimental data.

3. Results and Discussion

It is very important for the ferrocyanide-based ORFB to clarify the influence of different flow fields and different electrode configurations on the battery performance and the transport process. Three different electrode shapes (trapezoid, sector, and rectangle), with a surface area of 6400 mm^2 , are studied in the subsequent experiments, and the three electrodes are equipped with three flow fields. The geometry data for the different electrodes and the flow fields are listed in Table 3. The flow fields and the electrodes are presented in Figure 1. The contact areas between the flow field with the electrode for the three ferrocyanide-based ORFBs remain the same. The battery performance and mass transfer behaviors of the three the ferrocyanide-based ORFBs are obtained, which is important for the ferrocyanide-based ORFB application.

Table 3. Geometric and operation parameters used in the simulation.

| Parameter | Symbol | Value |
|--|-----------------------------------|--------|
| Length of the electrode (mm) | L_e | 80 |
| Width of the electrode (mm) | W_e | 80 |
| Height of the electrode (mm) | H_e | 3.5 |
| Length of the membrane (mm) | L_m | 80 |
| Width of the membrane (mm) | W_m | 80 |
| Height of the membrane (mm) | H_m | 0.2 |
| Width of the flow field (mm) | W_c | 3.5 |
| Height of the flow field (mm) | H_c | 3.5 |
| Length of spindle electrode (mm) | L_c | 642.91 |
| Initial concentration of 2,6-reDHAQ (mol/m^3) | $c_{2,6\text{-reDHAQ}}$ | 20 |
| Initial concentration of 2,6-DHAQ (mol/m^3) | $c_{2,6\text{-DHAQ}}$ | 180 |
| Initial concentration of $\text{Fe}(\text{CN})_6^{4-}$ (mol/m^3) | $c_{\text{Fe}(\text{CN})_6^{4-}}$ | 40 |
| Initial concentration of $\text{Fe}(\text{CN})_6^{3-}$ (mol/m^3) | $c_{\text{Fe}(\text{CN})_6^{3-}}$ | 360 |
| K^+ concentration in half-cell (mol/m^3) | c_{K^+} | 1500 |
| OH^- concentration in half-cell (mol/m^3) | c_{OH^-} | 1500 |
| Porosity of the electrode | ε | 0.7 |
| Applied current density (mA/cm^2) | I | 40 |
| Inlet electrolyte flow rate (mL/min) | Q_0 | 600 |

3.1. Battery Performance of Batteries with Different Electrode Shapes

The battery performance (such as the charging-discharging voltage, overvoltage, and polarization) is the most important parameter to evaluate the ferrocyanide-based ORFBs. It is of benefit to point out the influences of the electrode shapes on the charging-discharging voltage. The variations in the charge and discharge voltage for the three kinds of batteries is shown in Figure 3, which shows that the trapezoid battery possesses the highest discharge voltage during the discharge process. In the charging process, the trapezoid battery requires the lowest charge voltage. The discharge voltage of trapezoid battery is slightly higher than that of the sector battery, while the charging voltage of the sector battery is slightly higher than that of trapezoid battery. The charging voltage of rectangle battery is the highest, reaching the highest value at SOC = 0.9, which is 3.46% higher than that of the trapezoid battery. The discharge voltage of the rectangle battery is the lowest, and its value reaches the lowest value at SOC = 0.9, which is 4.47% lower than the discharge voltage of the trapezoid battery.

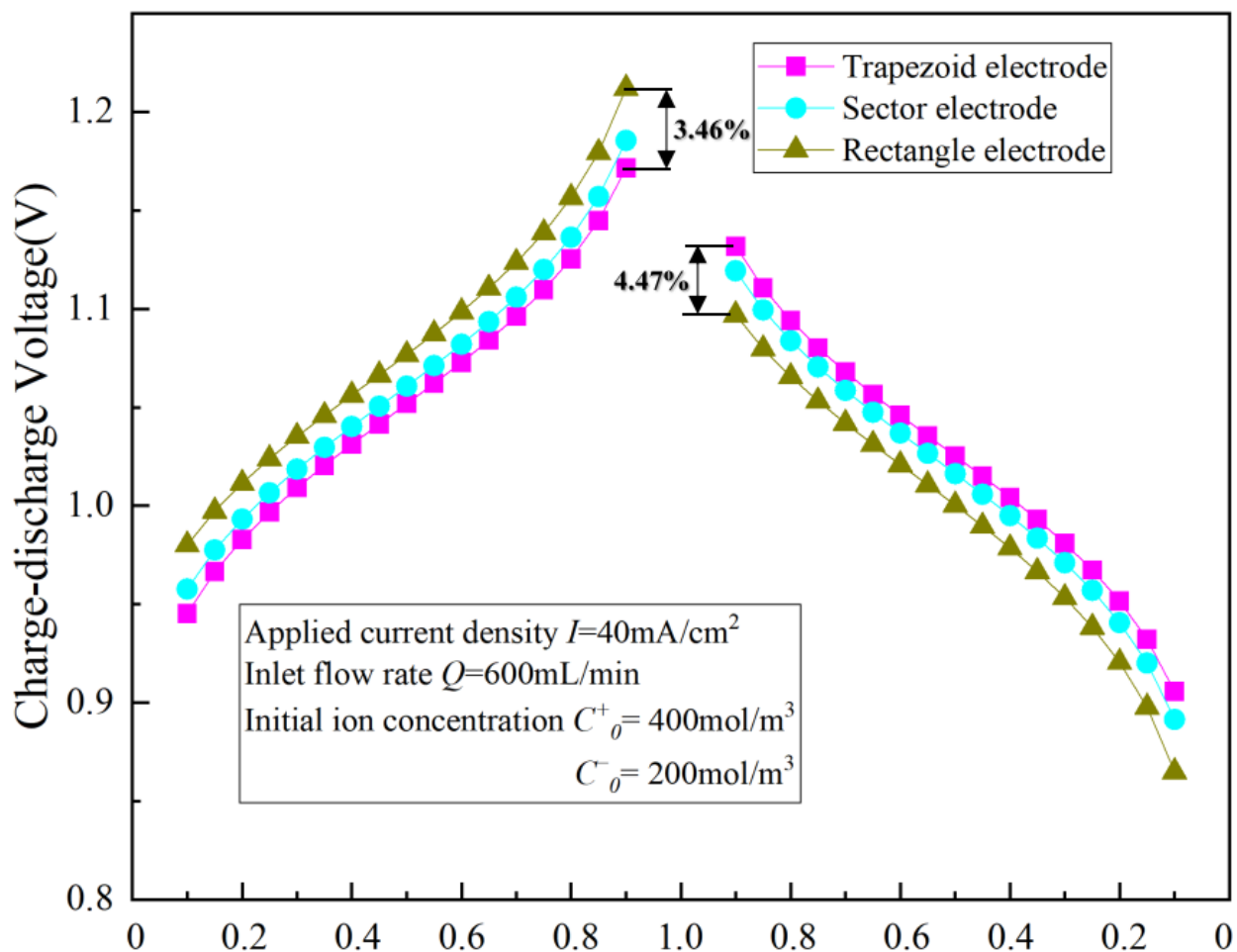


Figure 3. Variations in the charge-discharge voltages for the ferrocyanide-based ORFBs with different electrodes.

Presented in Figure 4, the overvoltage is also a key parameter, which increased in the numerical model. The overvoltage variation in the three different batteries during the discharge process can be seen in Figure 4. Figure 4 shows that the absolute value of overvoltage decreases first and then increases with the increase in SOC, which is due to the lack of reactants and products. In addition, Figure 4 shows that the trapezoid battery has the lowest absolute value of overvoltage during the discharge process, both for the

negative and positive electrodes. Therefore, the trapezoid battery can achieve the highest discharge voltage for the ferrocyanide-based ORFB.

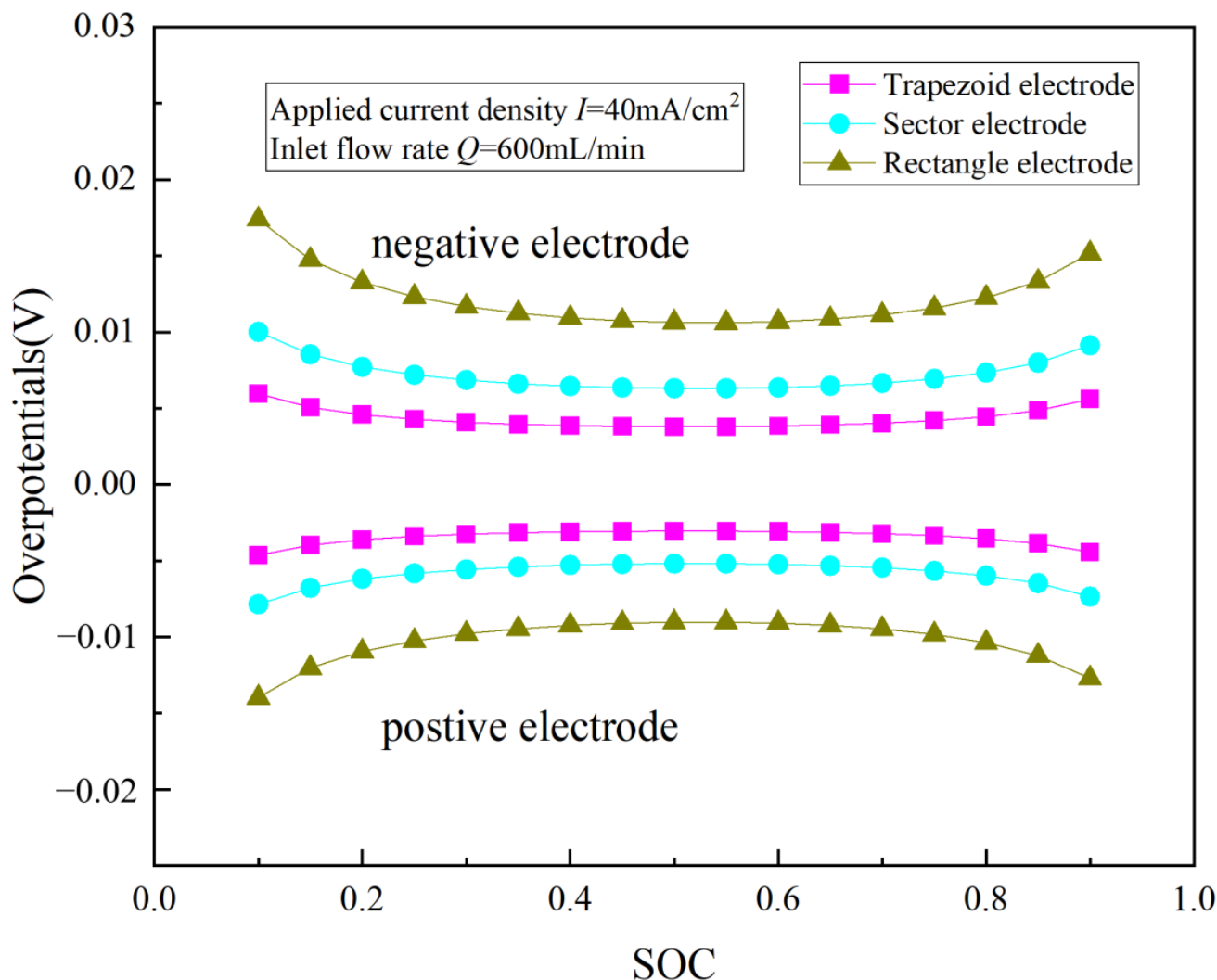


Figure 4. Variations in electrode overpotentials during discharge process using different electrodes.

In addition, the polarization is also an important factor influenced by the transport process. Figure 5 shows the variations in the polarization under the SOC = 0.8 condition, illustrating that the discharge voltage decreases as the current density increases for the three kinds of batteries. When the current density is set to 40 mA/cm², the discharge voltage of the trapezoid battery is 33.76% higher than the discharge voltage of the rectangle battery. The lower the polarization loss, the higher the discharge voltage, which illustrates that the battery performance of the trapezoid battery is the best.

3.2. Mass Transfer Behaviors of Batteries with Different Electrode Shapes

Mass transfer behavior is one of the important factors affecting the performance of the battery. In this paper, the mass transfer behaviors of three batteries are quantitatively investigated using the uniformity factor. The variations in the uniformity factor during the discharge process are shown in Figure 6, which shows that the concentration distribution of the electrolyte in the trapezoid battery is more uniform than that of the other batteries. Particularly, when SOC = 0.1, the uniformity factor value of the trapezoid battery is 26.9% higher than that of the rectangle battery. The electrolyte contribution distributes more uniformly, and better battery performance can be achieved, which is consistent with the previous conclusion. Therefore, the trapezoid battery exhibits better mass transfer behavior.

In addition, it is not difficult to see that the uniformity factors of the three batteries show a downward trend during the discharge process (SOC from 0.9 to 0.1), according to Figure 6. When the SOC is low, there is a poor mass transfer performance and nonuniformity concentration distribution in the battery, which results in low battery performance.

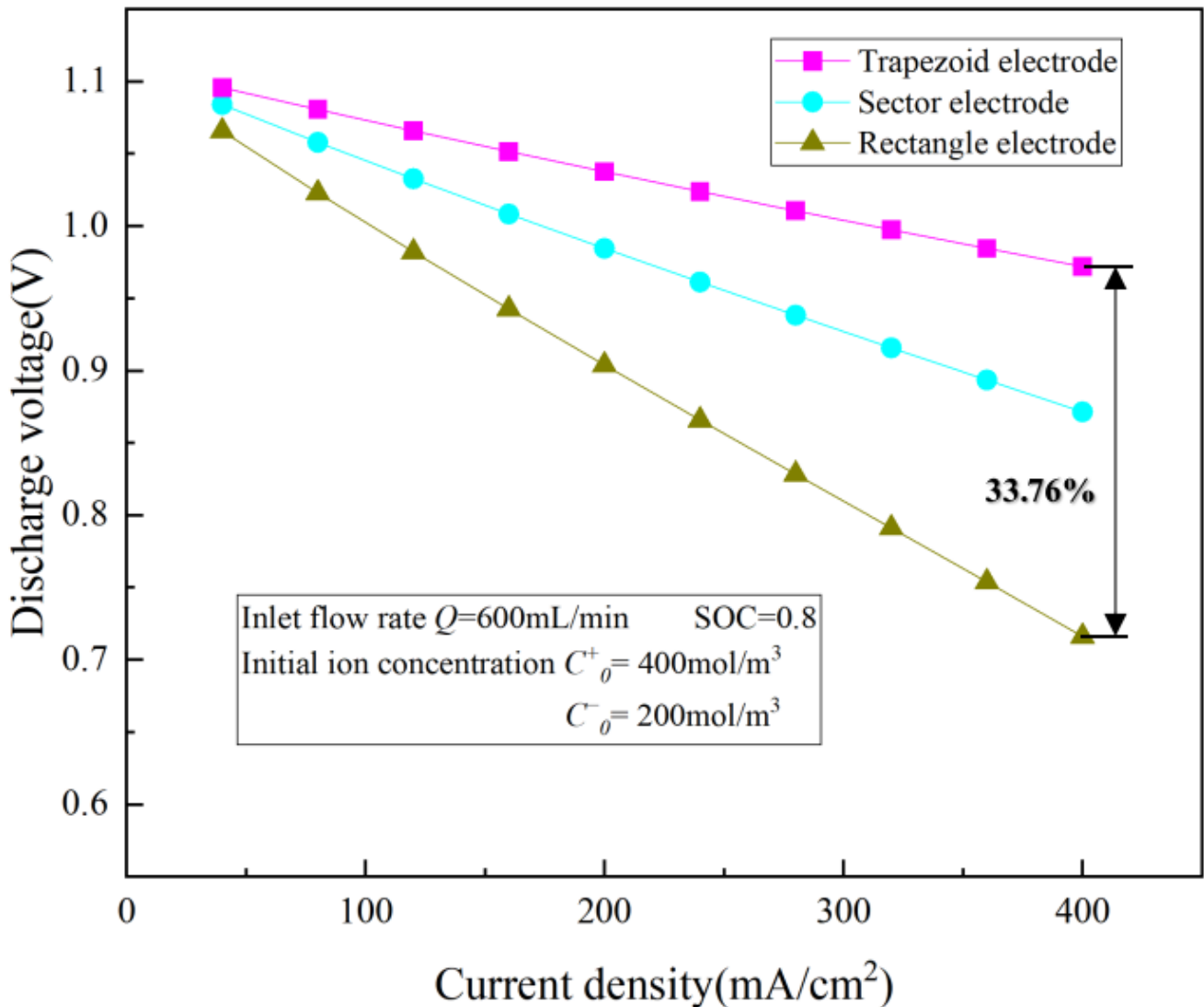


Figure 5. Polarization curve of different flow fields.

It is well known that the active ion concentration is one of the important conditions for changing and discharging the overvoltage. In order to accurately and clearly evaluate the distribution of the active ion concentration, the negative electrode is divided into four equal parts along the electrode thickness direction, as shown in Figure 7. The concentration of 2,6-reDHAQ is taken as the representative of the active ions concentration in this section. Figure 8 (SOC = 0.2) and Figure 9 (SOC = 0.6) show the distribution of the 2,6-reDHAQ concentration in the 3L/4 plate of different batteries. It is not difficult to see that the 2,6-reDHAQ concentration of the trapezoid battery is the highest, and the 2,6-reDHAQ distribution of the trapezoid battery is the most uniform.

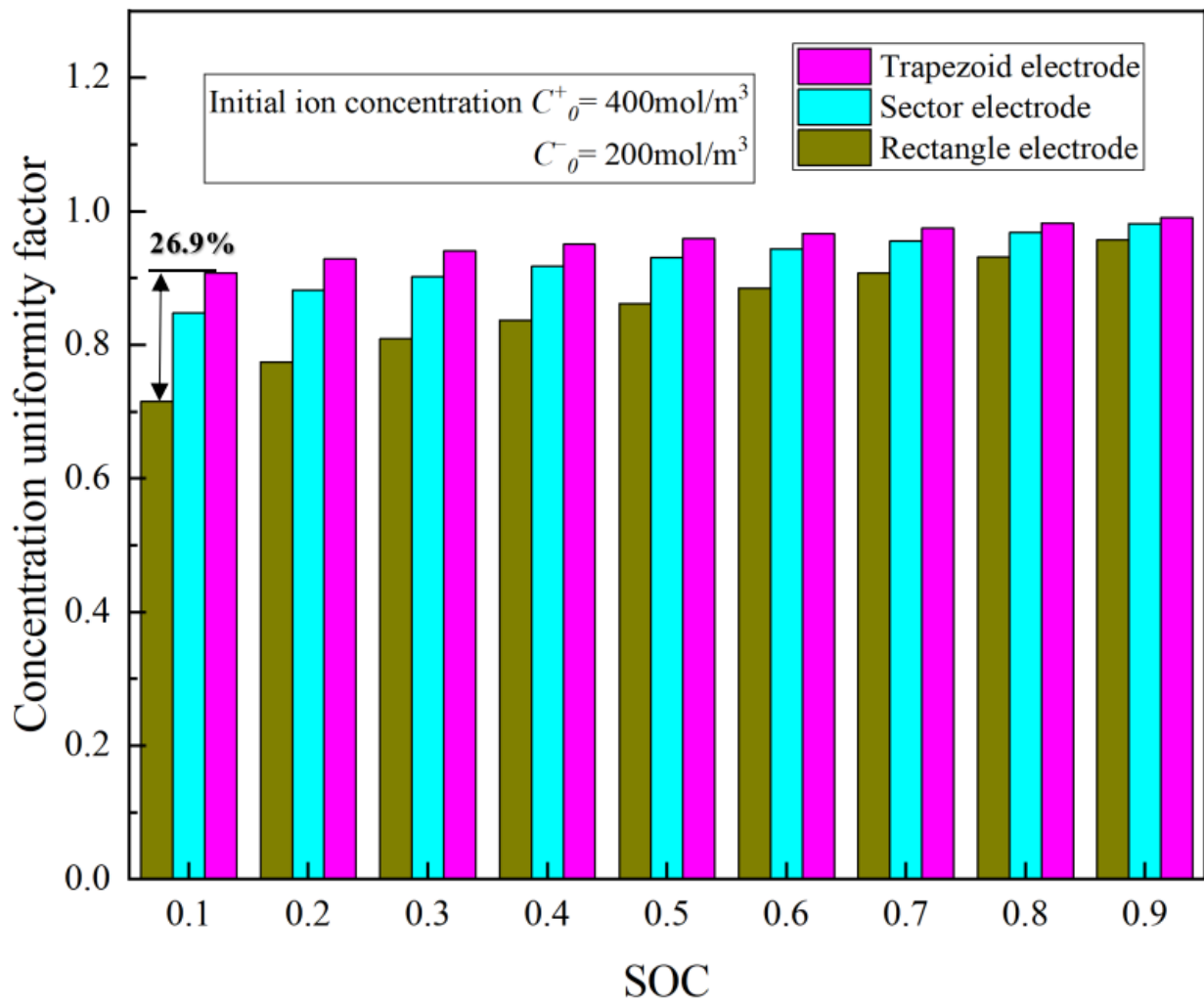


Figure 6. Variations in the uniformity factor during the discharge process under different flow fields.

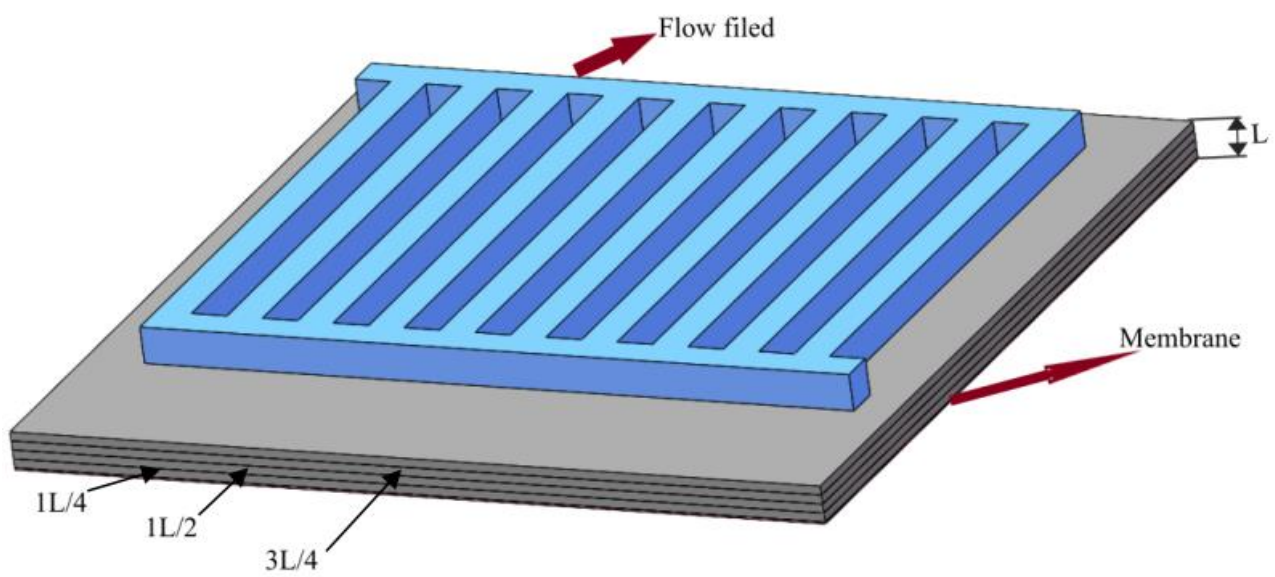


Figure 7. Diagram of the electrode sections.

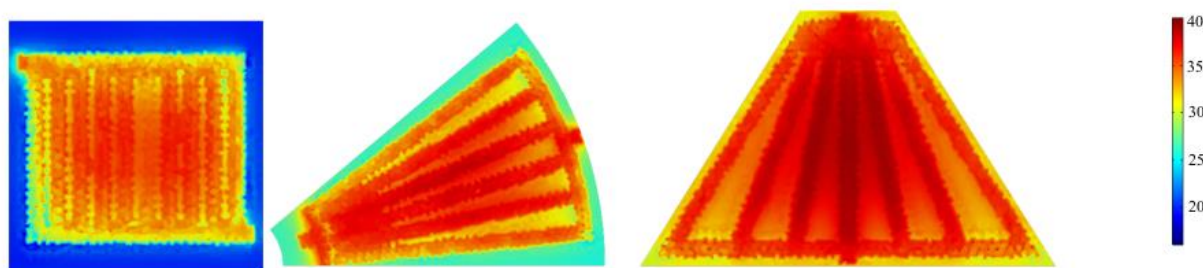


Figure 8. The 2,6-reDHAQ concentration distribution of the 3L/4 cut plane at 0.2 SOC.

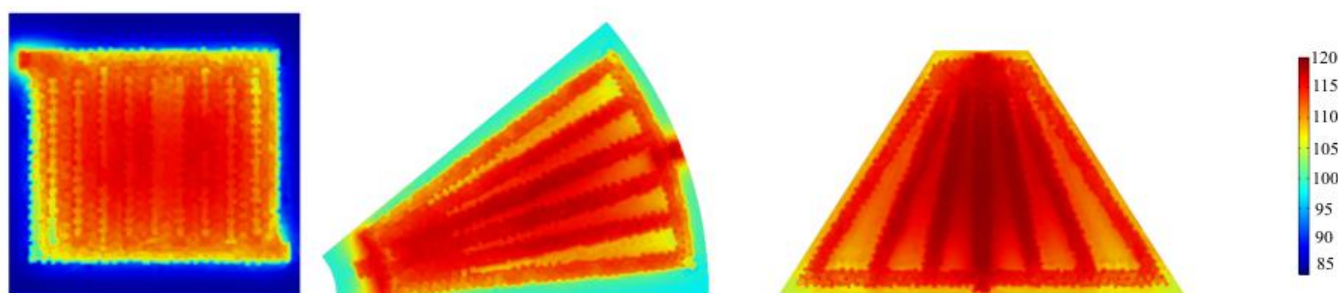


Figure 9. The 2,6-reDHAQ concentration distribution of the 3L/4 cut plane at 0.6 SOC.

For quantitatively evaluating the concentration distribution in different batteries, Figures 10 and 11 show the average concentration variations of 2,6-reDHAQ for the three batteries in different plates under the conditions of SOC = 0.2 and SOC = 0.6. It can be seen from Figures 10 and 11 that the concentration of 2,6-reDHAQ increases when moving from 1L/4 to 3L/4, which is the result of flow resistance. Whether in SOC = 0.2 or SOC = 0.6, the average concentration of the trapezoid section is the highest, under any condition. Therefore, the trapezoid battery can enhance the transport of active ions, so that the trapezoid battery can obtain better performance.

3.3. Power Performance of Batteries with Different Electrode Shapes

The hydrodynamic characteristics of different electrodes will result in different pressure drops. Figure 12 shows the variations in pressure drop for the negative electrode from a 600 mL/min flow rate to a 1200 mL/min flow rate. The pressure drop of the trapezoid battery is the lowest, while the pressure drop of the rectangle battery is the highest. At the flow rate of 1200 mL/min, the pressure drop of the rectangle battery is 3520 Pa higher than that of trapezoid battery. Taking the loss of pump work into account, Figure 13 shows the variations in the net power with the flow rate for the three batteries, which illustrates that the net power of the trapezoid battery remains the highest as the flow rate increases from 600 mL/min to 1200 mL/min. Under the flow rate condition of 600 mL/min, the power of the trapezoid battery is 7.58% higher than that of the rectangle battery. Figure 14 shows the variations in the power-based efficiency with the increase in the flow rate for the three batteries, from which it can be seen that the efficiency based on the power of the trapezoid electrode is the highest. Therefore, the trapezoid battery can achieve the best net output power. At the flow rate of 10 mL/s, the efficiency of the trapezoid battery is 4.96% higher than that of the rectangle battery. Therefore, the performance of the trapezoid battery is better than that of the rectangle battery.

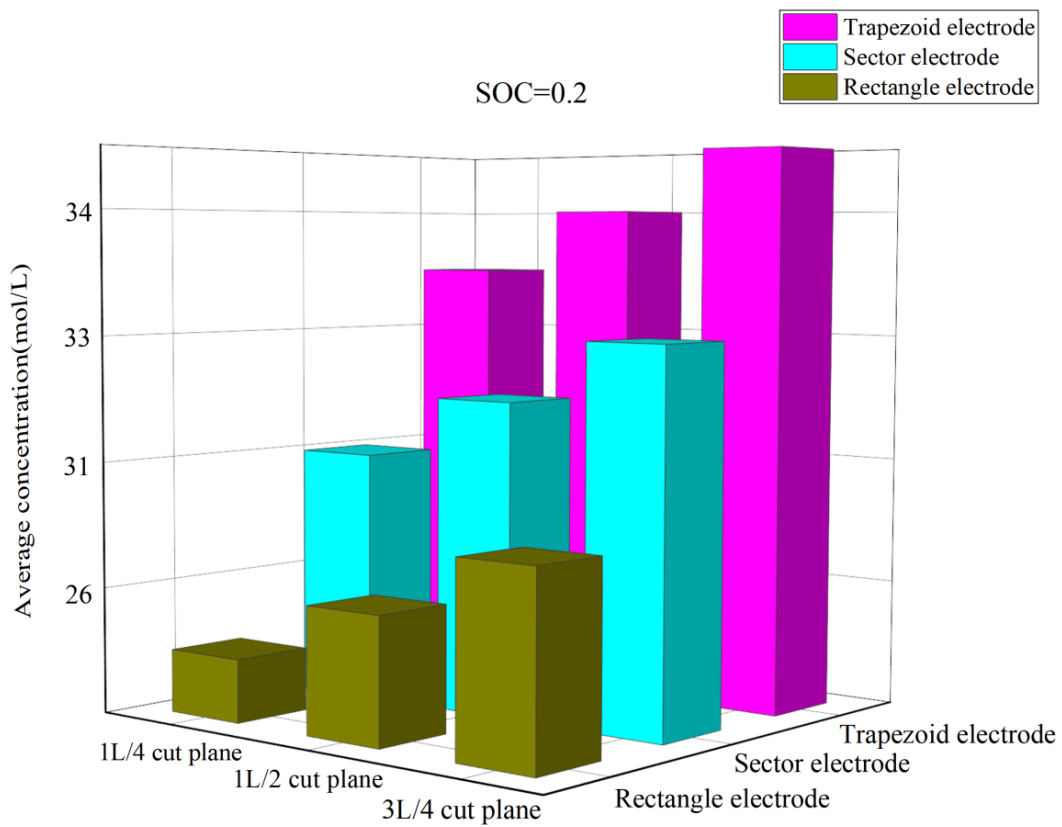


Figure 10. Average concentration of different batteries at different slice positions and at 0.2 SOC.

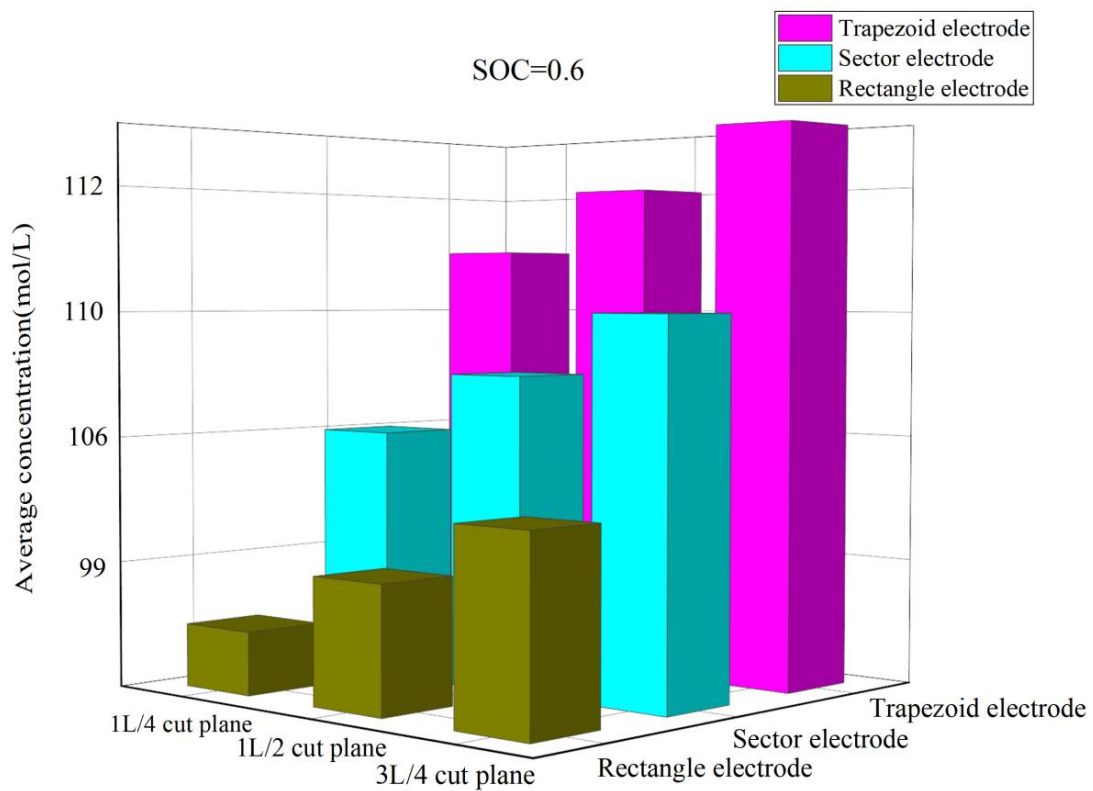


Figure 11. Average concentration of different batteries at different slice positions and at 0.6 SOC.

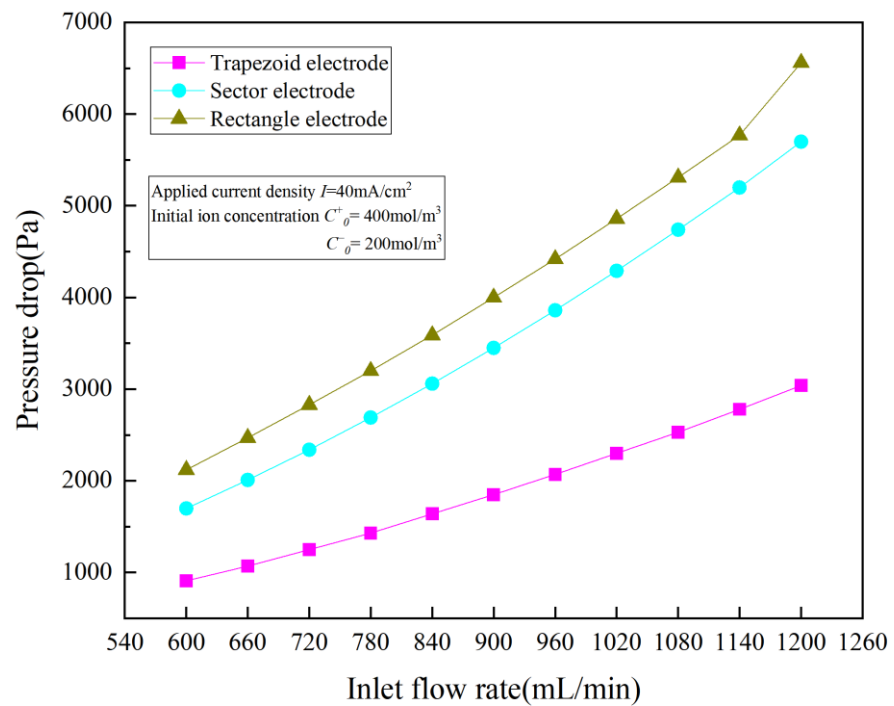


Figure 12. Variations in pressure drops with inlet flow rates under different electrodes.

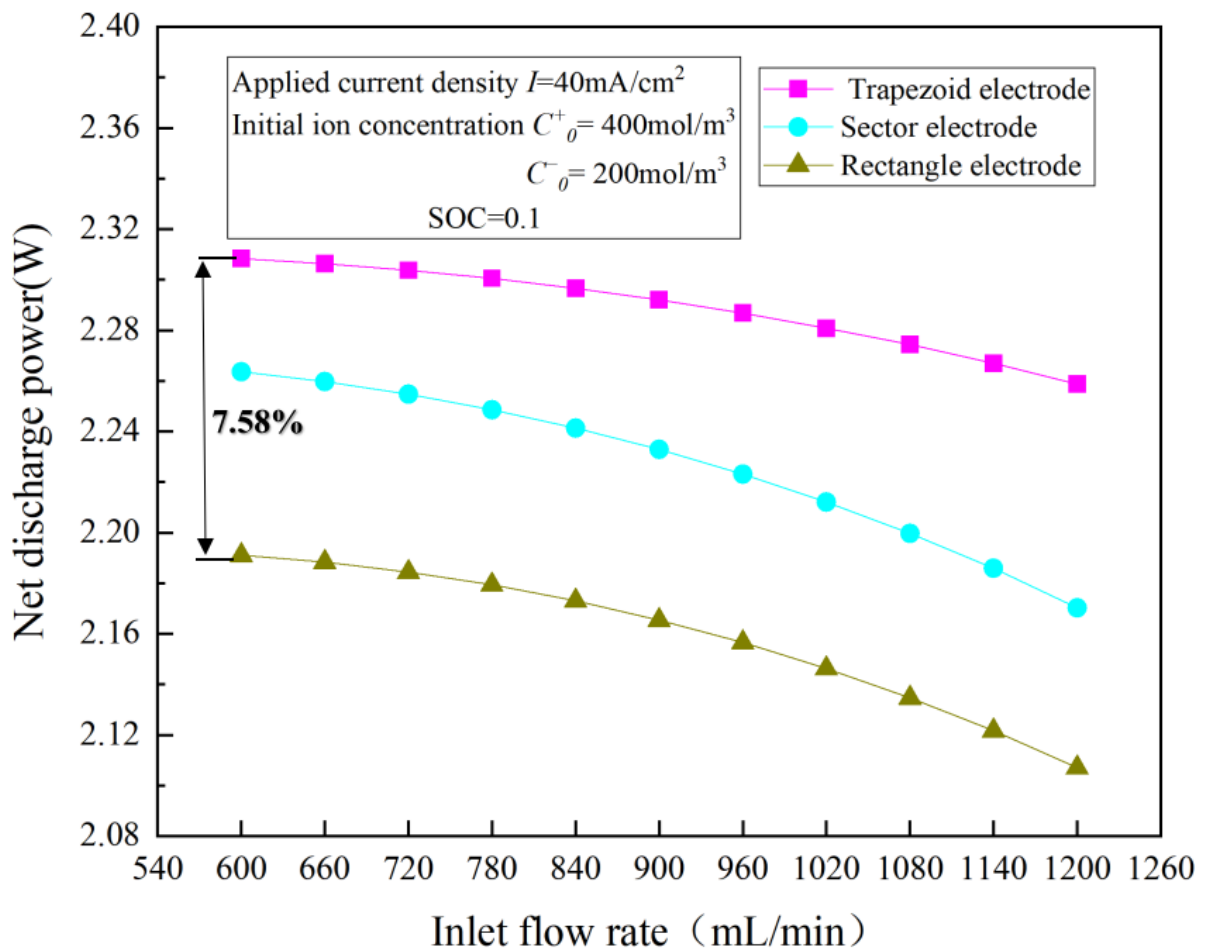


Figure 13. Variations in net discharge power with the electrolyte flow rates.

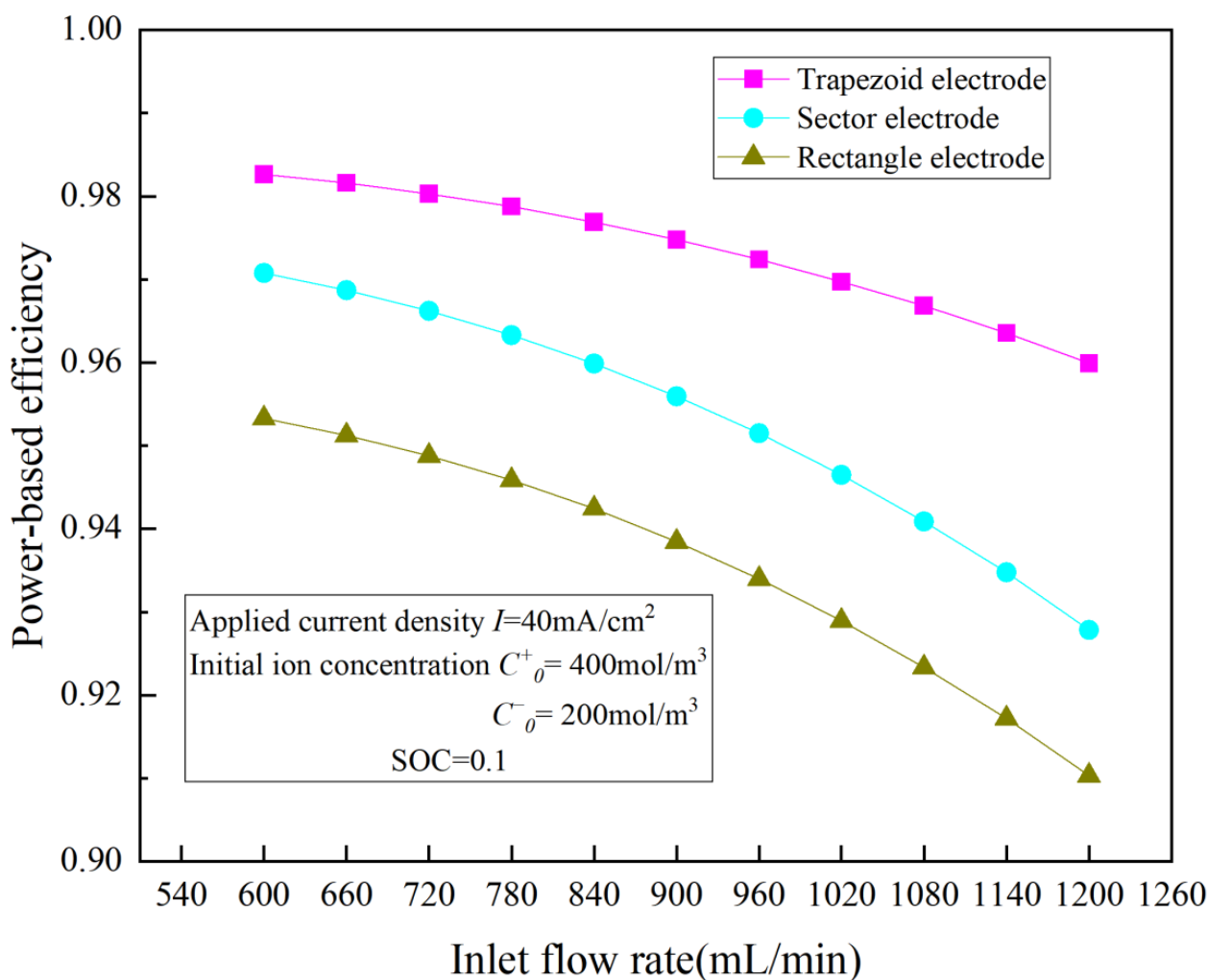


Figure 14. Variations in power efficiency with inlet concentration.

4. Conclusions

In this paper, the mass transfer and battery performance of three electrodes (trapezoid, sector, and rectangle), with flow fields, are studied based on a numerical model, which is verified by the experiments. The results show that the discharge voltage of the ferrocyanide-based ORFB with a trapezoid electrode is highest, and that with the rectangle electrode is lowest, and the ferrocyanide-based ORFB with a trapezoid electrode requires the lowest charge voltage. The charging voltage of the rectangle battery is the highest, and the charging voltage of the trapezoid battery is the lowest. The charging voltage of the rectangle battery is 3.46% higher than that of the trapezoid battery at SOC = 0.9. The discharge voltage of rectangle battery is the lowest, and the discharge voltage of the trapezoid battery is the highest. The discharge voltage of the rectangle battery is 4.47% lower than that of the trapezoid battery. The uniformity factor value of the trapezoid battery is 26.9% higher than that of the rectangle battery, and the power of the trapezoid battery is 7.58% higher than that of the rectangle battery. Therefore, the trapezoid shape is the best design for the electrodes of the ferrocyanide-based ORFBs.

Author Contributions: Writing—Original Draft, P.Z.; Software—Validation, X.L.; Supervision, J.F.; Writing—Review & Editing, F.C. All authors have read and agreed to the published version of the manuscript.

Funding: The financial support from the Beijing Natural Science Foundation(3232025) and National Natural Science Foundation of China (Grant No. 51906012). Support from the Fundamental Research Funds for the Central Universities (BUCTRC201922).

Data Availability Statement: The data used to support the findings of this study are available from the corresponding author upon request.

Conflicts of Interest: The authors declare no conflict of interest.

References

1. Dunn, B.; Kamath, H.; Tarascon, J.M. Electrical energy storage for the grid: A battery of choices. *Science* **2011**, *334*, 928–935. Available online: <https://www.science.org/doi/10.1126/science.1212741> (accessed on 15 January 2023). [CrossRef]
2. Zhang, H.S.; Hao, R.J.; Liu, X.; Zhang, N.; Guo, W.; Zhang, Z.; Liu, C.; Liu, Y.; Duan, C.H.; Qin, J.Y. Thermodynamic performance analysis of an improved coal-fired power generation system coupled with geothermal energy based on organic Rankine cycle. *Renew. Energ.* **2022**, *201*, 273–290. [CrossRef]
3. Liu, H.; Ye, C.; Ye, Z.; Zhu, Z.; Wang, Q.; Tang, Y.; Luo, G.; Guo, W.; Dong, C.; Li, G.; et al. Catalytic cracking and catalyst deactivation/regeneration characteristics of Fe-loaded biochar catalysts for tar model compound. *Fuel* **2023**, *334*, 126810. [CrossRef]
4. Sun, T.F.; Fan, Y.C.; Liu, X.; Fu, J.J.; Tan, Z.A.; Chu, F.M. Battery performance promotion and mass transfer enhancement of organic redox flow battery by a novel spindle electrode design. *Chem. Eng. J.* **2023**, *462*, 142197. [CrossRef]
5. Poizot, P.; Gaubicher, J.; Renault, S.; Dubois, L.; Yan, L.L.; Yao, Y. Opportunities and challenges for organic electrodes in electrochemical energy storage. *Chem. Rev.* **2020**, *120*, 6490–6557. [CrossRef] [PubMed]
6. Wang, F.; Xiao, G.; Chu, F. Mass transfer enhancement in electrode and battery performance optimization of all-vanadium flow based on channel section reconstruction. *Chem. Eng. J.* **2023**, *451*, 138619. [CrossRef]
7. He, H.Y.; Tian, S.; Tarroja, B.; Ogunseitan, O.A.; Samuelsen, S.; Schoenung, J.M. Flow battery production: Materials selection and environmental impact. *J. Clean. Prod.* **2020**, *269*, 121740. [CrossRef]
8. Winsberg, J.; Hagemann, T.; Janoschka, T.; Hager, M.D.; Schubert, U.S. Redox-flow batteries: From metals to organic redox active materials. *Angew. Chem. Int. Edit.* **2017**, *56*, 686–711. [CrossRef]
9. Su, L.; Andres, F.B.; Chang, S.C.; Jesse, J.H.; Fikile, R.B. Toward an inexpensive aqueous polysulfide-polyiodide redox flow battery. *Ind. Eng. Chem. Res.* **2017**, *56*, 9783–9792. [CrossRef]
10. Houser, J.; Pezeshki, A.; Clement, J.T.; Aaron, D.; Mench, M.M. Architecture for improved mass transport and system performance in redox flow batteries. *J. Power Sources* **2017**, *351*, 96–105. Available online: <https://www.sciencedirect.com/science/article/abs/pii/S0378775317303816> (accessed on 15 January 2023). [CrossRef]
11. Xu, Q.; Zhao, T.S.; Leung, P.K. Numerical investigations of flow field designs for vanadium redox flow batteries. *Appl. Energ.* **2013**, *105*, 47–56. Available online: <https://www.sciencedirect.com/science/article/abs/pii/S0306261912009324> (accessed on 15 January 2023). [CrossRef]
12. Macdonald, M.; Darling, R.M. Comparing velocities and pressures in redox flow batteries with interdigitated and serpentine channels. *Aiche. J.* **2019**, *65*, 5. [CrossRef]
13. Luo, Y.S.; Zheng, M.L.; Sun, J. Model-based optimization for combined interdigitated and serpentine flow field in redox flow batteries. *Int. J. Green Energy* **2022**, *1543–5075*, 1–12. [CrossRef]
14. Ali, E.; Kwon, H.; Kim, J.; Park, H. Numerical study on serpentine design flow channel configurations for vanadium redox flow batteries. *J. Energy Storage* **2020**, *32*, 101802. [CrossRef]
15. Lu, M.Y.; Jiao, Y.H.; Tang, X.Y.; Yang, W.W.; Ye, M.; Xu, Q. Blocked serpentine flow field with enhanced species transport and improved flow distribution for vanadium redox flow battery. *J. Energy Storage* **2021**, *35*, 102284. [CrossRef]
16. Lee, J.; Kim, J.; Park, H. Numerical simulation of the power-based efficiency in vanadium redox flow battery with different serpentine channel size. *Int. J. Hydrog. Energy* **2019**, *44*, 29483–29492. [CrossRef]
17. Chu, F.; Su, M.; Xiao, G.; Tan, Z.; Yang, G. Analysis of electrode configuration effects on mass transfer and organic redox flow battery performance. *Ind. Eng. Chem. Res.* **2022**, *61*, 2915–2925. [CrossRef]
18. Yin, C.; Gao, Y.; Xie, G.; Li, T.; Tang, H. Three dimensional multi-physical modeling study of interdigitated flow field in porous electrode for vanadium redox flow battery. *J. Power Sources* **2019**, *438*, 227023. Available online: <https://www.sciencedirect.com/science/article/abs/pii/S037877531931016X?via%3Dihub> (accessed on 15 January 2023). [CrossRef]
19. Gurieff, N.; Cheung, C.Y.; Timchenko, V.; Menictas, C. Performance enhancing stack geometry concepts for redox flow battery systems with flow through electrodes. *J. Energy Storage* **2019**, *22*, 219–227. Available online: <https://www.sciencedirect.com/science/article/abs/pii/S2352152X18305905> (accessed on 17 January 2023). [CrossRef]
20. Ali, E.; Kwon, H.; Choi, J.; Lee, J.; Kim, J.; Park, H. A numerical study of electrode thickness and porosity effects in all vanadium redox flow batteries. *J. Energy Storage* **2020**, *28*, 101208. Available online: <https://www.sciencedirect.com/science/article/abs/pii/S2352152X19313301> (accessed on 17 January 2023). [CrossRef]
21. Lu, M.Y.; Yang, W.W.; Bai, X.S.; Deng, Y.M.; He, Y.L. Performance improvement of a vanadium redox flow battery with asymmetric electrode designs. *Electrochim. Acta* **2019**, *319*, 210–226. Available online: <https://www.sciencedirect.com/science/article/abs/pii/S0013468619313015> (accessed on 17 January 2023). [CrossRef]

22. Luo, J.; Sam, A.; Hu, B.; DeBruler, C.; Wei, X.; Wang, W.; Liu, T.L. Unraveling pH dependent cycling stability of ferricyanide/ferrocyanide in redox flow batteries. *Nano Energy* **2018**, *42*, 215–221. [CrossRef]
23. Chu, F.M.; Xiao, G.Z. Analysis of battery performance and mass transfer behavior for organic redox flow battery with different flow fields. *J. Electrochem. Soc.* **2022**, *169*, 070529. [CrossRef]
24. Lin, K.; Chen, Q.; Gerhardt, M.R.; Tong, L.; Kim, S.B.; Eisenach, L.; Valle, A.W.; Hardee, D.; Gordon, R.G.; Aziz, M.J.; et al. Alkaline quinone flow battery. *Science* **2015**, *349*, 1529–1532. Available online: <https://www.science.org/doi/full/10.1126/science.aab3033> (accessed on 18 January 2023). [CrossRef] [PubMed]

Disclaimer/Publisher’s Note: The statements, opinions and data contained in all publications are solely those of the individual author(s) and contributor(s) and not of MDPI and/or the editor(s). MDPI and/or the editor(s) disclaim responsibility for any injury to people or property resulting from any ideas, methods, instructions or products referred to in the content.